Materials Research Bulletin 122 (2020) 110645

Contents lists available at ScienceDirect

Materials Research Bulletin

journal homepage: www.elsevier.com/locate/matresbu

Tuning electronic and photocatalytic properties in pulsed light synthesis of Cu_2ZnSnS_4 films from CuS-ZnS-SnS nanoparticles

Hyun-Jun Hwang[a,1], Cheng Zeng[b,1], Changqing Pan[b,1], Michael Dexter[a], Rajiv Malhotra[a,*], Chih-hung Chang[b,*]

[a] Department of Mechanical and Aerospace Engineering, Rutgers University, 98 Brett Road, Piscataway Township, NJ 08854, USA
[b] School of Chemical, Biological, and Environmental Engineering, Oregon State University, Corvallis, OR, 97331, USA

ARTICLE INFO

Keywords:
Cu_2ZnSnS_4
Binary nanoparticles
Intense pulsed light synthesis
Photocatalyst

ABSTRACT

We investigate rapid in-situ synthesis of Cu_2ZnSnS_4 (CZTS) thin films via Intense Pulsed Light (IPL) irradiation of solution-deposited and mixed binary CuS, ZnS, SnS nanoparticles (NPs) in ambient conditions. The film phase, composition, morphology, electrical properties, optical properties and photocatalytic activity are characterized as a function of the optical fluence. Crystalline pure-phase kesterite CZTS films with high p-type conductivity of 51 S/cm and optical band gap 1.42 eV are synthesized within 15 s. Surprisingly, using supra-optimal IPL fluence (in 19 s) yields films with a composite CZTS-SnO_2/SnS_2 composition that exhibits about 20% higher photocatalytic efficiency and higher carrier mobility ($\approx$ 120 cm^2/Vs) than pure-phase kesterite films. The reaction pathways during IPL irradiation and the resulting film composition are used to understand the enhanced photocatalysis for the supra-optimal fluence. This work will create new avenues for scalable IPL-based bottom-up synthesis of new multinary chalcogenide composites from their binary NPs.

1. Introduction

P-type kesterite Cu_2ZnSnS_4 (CZTS) has a direct band gap range from 1.0 to 1.5 eV and a high absorption coefficient (10^4 cm^{-1}) in the visible spectrum [1,2]. Further, the constituent elements of CZTS are earth-abundant and non-toxic. Due to these favorable properties CZTS films are rapidly emerging as promising materials for applications such as absorber and photo-electrodes in solar cells [3–8], water splitting [9], CO_2 reduction [10], and degradation of dyes and organic pollutants [11,12]. A critical need to realizing these applications are rapid, large-area capable processes that utilize easily synthesized precursors to synthesize CZTS films of desired composition and phase.

CZTS films have been synthesized via methods such as thermal evaporation [13], pulsed laser deposition [14], Radio Frequency magnetron sputtering [15,16] and atom beam sputtering [17]. However, these vacuum-based methods require expensive and cumbersome equipment which limits their scalability. Solution phase CZTS nanoparticles (NPs) can be coated by ambient-condition and low-temperature approaches like aerosol-jet spray [18,19] and inkjet printing over large areas, thus promising greater scalability [20–23]. However, most of these approaches require sintering of the individual CZTS NPs to avoid excessive carrier recombination and scattering from the inter-NP boundaries [23,24]. Conventional oven sintering has limited scalability due to the need for high temperatures and relatively longer sintering time. For example, screen-printed CZTS NPs were found to need 400–500 °C for 30 min to 1 h [25] and aerosol-jet sprayed nanocrystals took similar times and temperatures even after pre-compaction [18,19]. Even Rapid Thermal Processing takes about 5–10 minutes at temperatures above 500 °C [26]. The small phase change window of CZTS and the tendency for metal sulfides to oxidize [27] makes it difficult to sinter CZTS NP films in air without creating undesirable intermediaries like Cu_2SnS_3, ZnO and Cu_7S_4 [28,29]. Thus, the films are usually placed in N_2 or H_2S environments inside closed chambers to control film composition, which further limits scalability by increasing the costs and the complication of the manufacturing process. Secondly, the synthesis of CZTS NPs with controlled phase and composition requires high degree of control of thermal and mass diffusion during synthesis. For example, it has been shown that the wurtzite phase of CZTS is the most favored phase in nanocrystals unless careful control of spatial crystal growth is achieved [30]. Various solution-based methods have been developed for synthesizing quaternary CZTS NPs [20–23]. However, the throughput of these processes is much lower than that for synthesis

* Corresponding authors.
E-mail addresses: rajiv.malhotra@rutgers.edu (R. Malhotra), chih-hung.chang@oregonstate.edu (C.-h. Chang).
[1] These authors contributed equally to this work.

https://doi.org/10.1016/j.materresbull.2019.110645
Received 23 March 2019; Received in revised form 23 September 2019; Accepted 23 September 2019
Available online 24 September 2019
0025-5408/

of binary metal NPs. For example, tabletop micromixer-based methods can synthesize each of the binary NPs (CuS, ZnS, SnS) that form the building blocks of CZTS at the rate of 320 gh^{-1} [23]. Further, the use of these binary NP precursors may also provide low temperature pathways for synthesis of CZTS films [31]. Thus, a significant advance will be realized by developing ambient-condition scalable approaches that can in-situ synthesize multinary CZTS films with controlled phase and composition from solution deposited binary NPs.

In Intense Pulsed Light (IPL) sintering broad-spectrum pulsed light from a xenon lamp is absorbed by the printed or coated NPs, resulting in NP heating and fusion. The key advantage of this process is ambient condition sintering within seconds and over large areas ($\geq$1 foot × 0.75 inch here) with minimal damage of the underlying substrate [32,33]. Past work has used IPL for physical fusion of pre-synthesized conductive (Ag [34,35], Ni [36], Cu [37]) and semiconductive (CdS [38], CuS [27], CdTe [39], TiO_2 [40], Cu(In,Ga)Se_2 (CIGSe) [41], Perovskites [42]) NPs. IPL of physically mixed Cu (In, Ga) NPs and Se NPs was used to synthesize CIGSe thin films [43] but required ternary metallic alloy NPs which are more difficult to synthesize. IPL can reduce metal salts dissolved in liquid-phase reducing agents to in-situ synthesize and fuse nanoparticles into metallic films [44] and perform dehydroxylation of metal hydroxides into amorphous metal oxide NP films [45,46]. The large-area and rapid nature of IPL suggests an inherent potential to achieve the aforementioned technological advance. Further, IPL has shown the ability to sinter metallic NPs like Nickel in ambient conditions without causing oxidation [36]. This implies the possibility to use IPL for fabrication of CZTS films without an inert-gas chamber.

However, this potential is unrealized primarily because there is limited work on IPL synthesis of multinary chalcogenide films from binary NP precursors under ambient conditions. This work investigates IPL synthesis of CZTS films from physically mixed and solution deposited ZnS, CuS and SnS NPs. The films' composition, morphology, optical and electrical properties, and photocatalytic degradation of Methylene Blue are characterized as a function of the IPL fluence. An optimal IPL fluence is found that produces pure-phase kesterite CZTS, with supra-optimal fluence yielding films that possess even greater carrier mobility and photocatalytic efficiency. The underlying reaction pathways and mechanisms behind these observations are discussed in detail.

2. Material and methods

2.1. Synthesis of binary nanoparticles mixture

ACS reagent grade copper(II) acetate ($Cu(OAc)_2$), zinc acetate ($Zn(OAc)_2$), tin(II) chloride ($SnCl_2$), sodium sulfide (Na_2S), monoethanolamine (MEA) were purchased from Sigma-Aldrich; as well as Polyvinylpyrrolidone (PVP, MW = 8000) from TCI America and thiourea (TU) from Alfa Aesar. All chemicals were used without further purification. The general approach to binary NP synthesis involved dissolving the above Cu, Zn, and Sn precursors in D.I. water, and mixing with a sulfur source (Na_2S) at the desired temperature, followed by burst precipitation and controlled growth of the binary NPs [47,48]. Fig. 1 illustrates the simple micromixer-based continuous flow precipitation process that was used to implement this approach in a scalable manner, after our previous work [23]. The concentrations of Cu $(OAc)_2$, $Zn(OAc)_2$, $SnCl_2$, and Na_2S were 0.25 M each. During synthesis of SnS, drops of HCl were added to $SnCl_2$ to inhibit hydrolysis. The binary NP inks were physically mixed together, with the introduction of MEA and PVP to form a stable NP mixture and prevent binary NP aggregation. After 2 h of ultrasonication the binary NP ink mixture was spin-coated on to glass substrates of size 1 inch × 1 inch in two consecutive layers at room temperature, and then vacuum dried. A TU layer (0.05 mol/L) was added on the coated film as an additional sulfur source to locally compensate for potential sulfur loss during IPL synthesis. All deposition was performed at room temperature.

2.2. Intense pulsed light synthesis

The coated mixed NP film was exposed to IPL in ambient air (Fig. 2a). This IPL system (Sinteron 3000, Xenon Corp.) consists of a xenon flash lamp with a rectangular optical footprint, lamp charging capacitors, a pulse controller and a sample stage to place the films on. The IPL used here has a broad power spectrum from 380 nm to 850 nm (Supplementary Information Fig. S1a) with most of the power in the visible spectrum. At a fixed distance from the lamp the pulse fluence depends on the pulse duration and the capacitor voltage [34]. In our experiments the samples were placed such that the optical footprint at the substrate location covered the entire substrate. The optical fluence was varied over three levels by controlling the pulse duration at a constant capacitor voltage of 3 kV, as listed in Table 1. The number of pulses was fixed at 10. The pulse off-time used was the minimum time needed for the capacitors to charge up between consecutive pulses and increased with greater pulse fluence. The total synthesis time also increased with the pulse fluence but was always less than 20 s. It is worth noting that these IPL parameters effectively fixed the irradiance per pulse at 6.9×10^3 W/cm^2. Therefore, increasing the IPL fluence basically resulted in the film being subjected to the same irradiance but for a longer pulse duration. The film temperature during IPL synthesis was measured using a high-speed laser pyrometer (Metis-M323) with radiant emissivity calibrated using a hot plate that was integrated with the sample holder, as in past work [34,49].

2.3. Characterization of film properties and photocatalytic activity

The crystal structure of the films was analyzed by X-ray diffraction (XRD) with a Bruker D8 Discover X-ray diffractometer. Raman spectra were obtained using WITec Alpha 300RA confocal Raman spectrometer with 514.5 nm excitation wavelength emitted from an Ar-ion laser. The film morphology was characterized using scanning electron microscopy (SEM, FEI Quanta 600 F) and transmission electron microscopy (TEM, FEI Titan 80-200). To prepare samples for the TEM study the NP mixture ink was drop cast on to Si_3N_4 grids followed by IPL synthesis. A Jasco V-670 UV–vis/NIR spectrophotometer, with a 150 mm integrating sphere for reflectivity measurements, was used to measure the UV–vis absorption of the films and the optical band gap. The electrical conductivity and charge carrier mobility were measured using an Ecopia HMS-5000 hall effect measurement system. The synthesis of the individual binary NPs was confirmed via Raman Spectroscopy, XRD and Energy-dispersive X-ray spectroscopy (EDX) of the corresponding films. The surface morphology was examined with a Bruker Innova atomic force microscope (AFM). STEM EDS mapping was performed (FEI Titan 80–200 TEM/ChemiSTEM) to clearly identify the phase of the composite film. The CZTS sample was dispersed on Ted Pella Pelco hydrophilic-coated silicon nitride membrane grid and subjected to IPL. EDS results at three areas were integrated by Bruker Esprit 1.9 and the spectra deconvoluted into C/N/O peaks with Lorentzian fitting.

Methylene Blue (MB), a cationic thiazine dye commonly used as a model compound to test photocatalytic degradation, was used to characterize photocatalytic efficiency of the synthesized film. Biological Stain Commission (BSC) certified MB dye was purchased from the J.T. Baker Chemical Company. The films were immersed in 10 mL of 1×10^{-6} mol/L MB solution and the setup was kept in dark for 30 min to achieve adsorption-desorption equilibrium of MB on the thin film surface. Then the setup was exposed to a simulated solar light source with Xenon arc lamp (Newport Oriel 96000) with a stirring bar as shown in Fig. 2b. The irradiation intensity was calibrated to 100 mW/cm^2 on the plane of the sample thin films. The degradation of the MB solution was measured as the change in the absorption spectra of the solution by using the Jasco V-670 spectrophotometer with 10 mm standard quartz cuvette in transmission mode. Measurements were

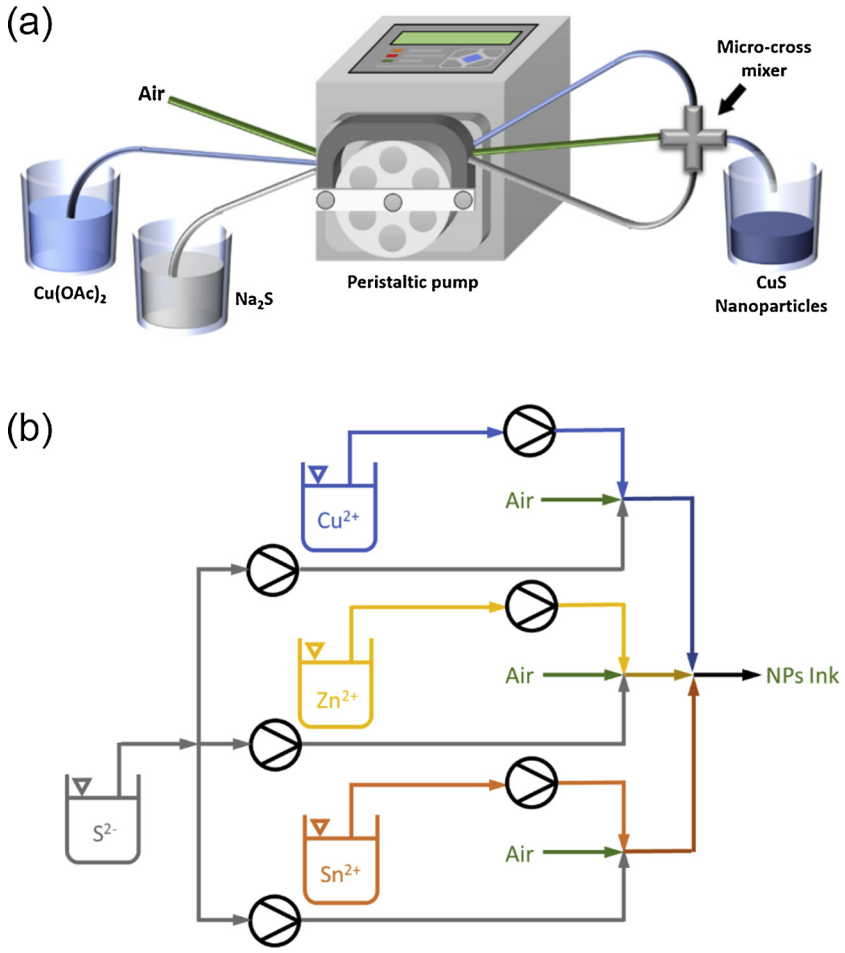

Fig. 1. (a) Schematic diagram of continuous precipitation process used, shown for synthesis of CuS NPs, and (b) flow chart of preparation of NP inks for film deposition.

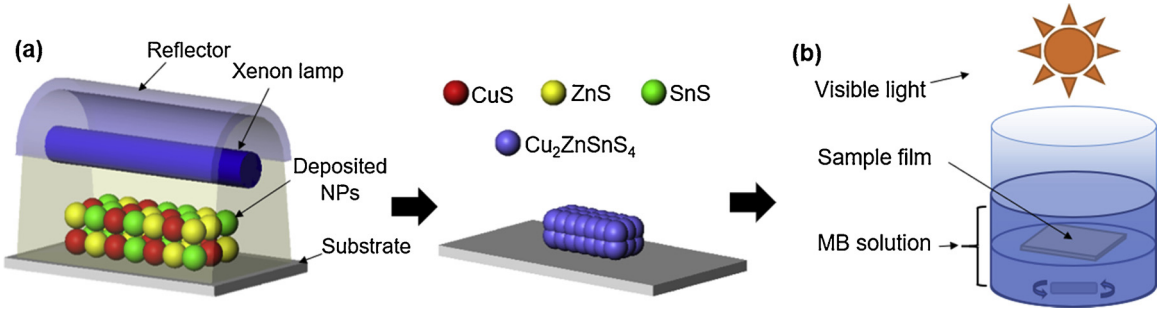

Fig. 2. Schematic of (a) IPL synthesis of mixed CuS, ZnS, SnS NPs for in-situ synthesis of CZTS (b) Characterization of photocatalytic activity of post-IPL films.

Table 1
IPL synthesis parameters used in experiments.

Fluence [J/cm^2]	Pulse duration [μs]	Pulse off-time [ms]	Total Synthesis time (s)
10	1430	990	9.9
16	2290	1515	15.2
20	2865	1900	19.0

performed for every 30 min for a total 4 h, and repeated for 4 times in order to check the reusability. MB has a characteristic absorption peak at 664 nm due to the n→π* transition. The measured evolution of intensity of this absorption peak was used to obtain the normalized change in MB concentration as C/C_0, where C_0 is the initial concentration of MB at the begin of irradiation, and C is the concentration of MB at an arbitrary time t. A lower value of C/C_0 over the same time period and with the same illumination intensity naturally implies greater photocatalytic efficiency. To examine the stability of the photocatalysis these measurements were also redone after an year. The kinetics of photodegradation of MB for this one-year later measurement was fitted to a pseudo- first-order reaction, $\ln(C_0/C) = k_{app}t$, where k_{app} is the apparent rate constant.

3. Results and discussion

3.1. Composition, crystallinity and morphology

The EDX spectra of the as-deposited mixed NP films in Fig. S1b

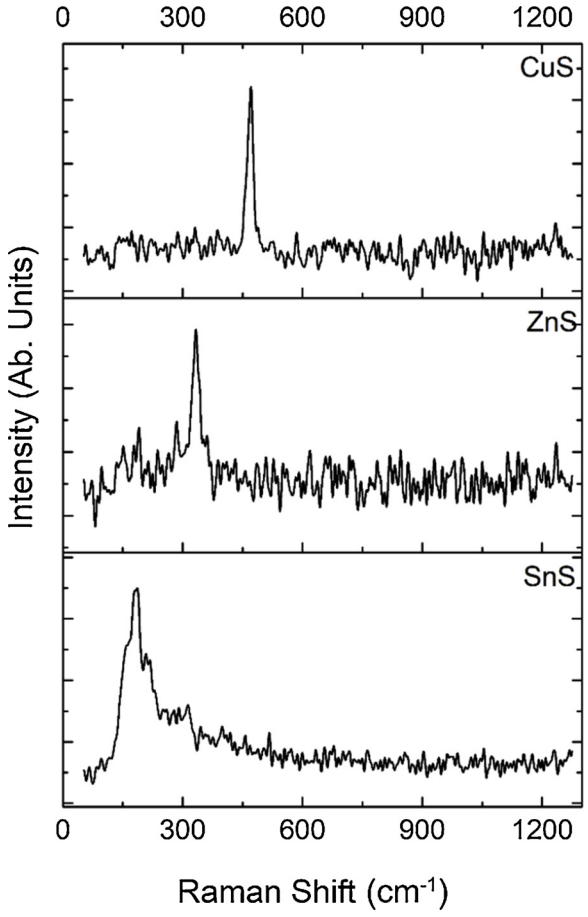

Fig. 3. Raman spectra of the binary NP films. CuS with peak at 470 cm^{-1}, ZnS with peak at 352 cm^{-1}, and SnS with peak at 189 cm^{-1}.

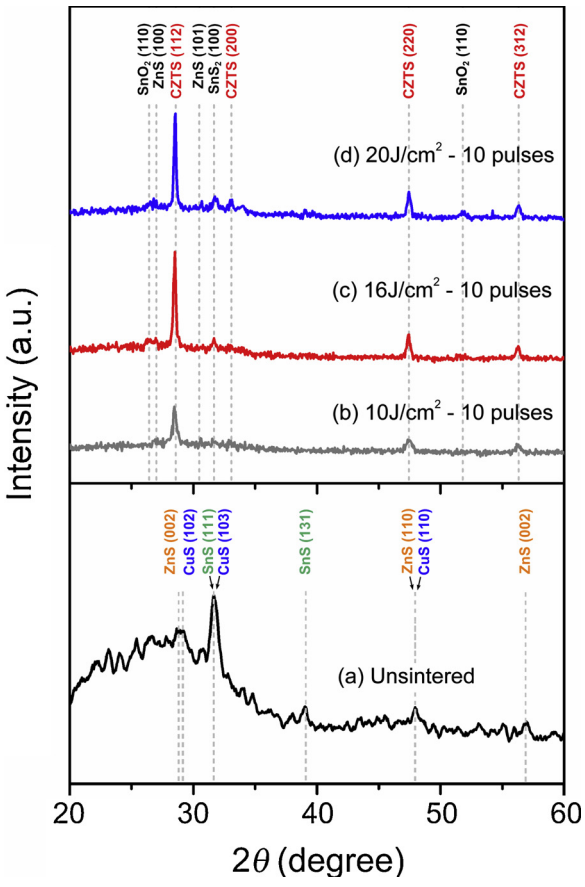

Fig. 4. XRD patterns of the quaternary CZTS nanoparticles films with varying IPL fluence (a) As-deposited, (b) 10 J/cm^2, (b) 16 J/cm^2, (c) 20 J/cm^2.

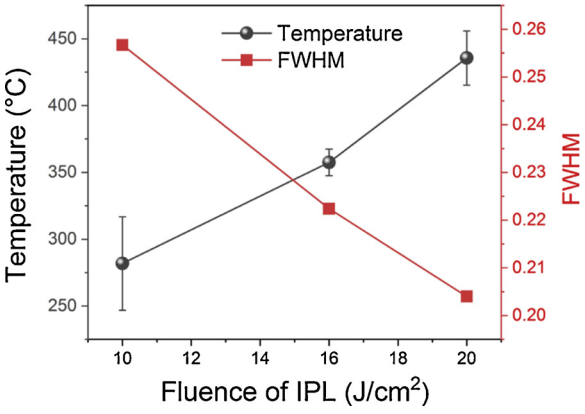

Fig. 5. Peak film temperature and FWHM of CZTS (112) XRD peak for varying IPL fluence.

(Supplementary Information) shows the presence of Cu, Sn, Zn and S. Further, the Raman spectra of the individual binary NP films in Fig. 3 confirm the synthesis of CuS (peak at 470 cm^{-1}) [50], ZnS (peak at 352 cm^{-1}) [51] and SnS (peak at 189 cm^{-1}) [52] NPs. The ratios of mixing of the individual binary NPs were adjusted so that the resulting Cu:Zn:Sn ratio in the mixed film was the stoichiometric value of 2:1:1.

Fig. 4a shows the XRD spectra of the mixed films before IPL synthesis, with peaks of SnS (111) and CuS (103) being visible but the rest of the peaks being less clear. The peak intensities for the as-deposited film were significantly lower than those for any of the IPL synthesized films, indicating much lower crystallinity of the as-deposited films. The CuS (JCPDS #39-0354), SnS (JCPDS #06-0464), and ZnS (JCPDS #79-2204) labels are provided for reference. The XRD patterns of the post-IPL films in Fig. 4b–d illustrate the effect of IPL fluence. For 10 J/cm^2 kesterite CZTS (JCPDS #26-0575) seems to be formed as indicated by the (112, 220, 312) peaks set at $2\theta = 28.53°$, 47.33°, and 56.18° respectively in Fig. 4b. The corresponding peak film temperature is 275 °C (Fig. 5). Increasing the fluence to 16 J/cm^2 increases the peak film temperature to above 350 °C and yields kesterite CZTS with greater crystallite size (smaller FWHM of primary (112) peak in Fig. 5). A smaller but distinguishable SnS_2 (100) peak at $2\theta = 31.8°$ (JCPDS #23-0677) also indicates the formation of some amount of SnS_2. SnO_2 (100) and wurtzite ZnS (100) peaks that are equally hard to distinguish and are of similarly lower intensity are observed at $2\theta = 26.3°$ and 27° (JCPDS #41-1445 and #79-2204 respectively). Increasing the fluence further to 20 J/cm^2 increases the peak temperature to 430 °C and reduces the FWHM of the primary kesterite CZTS peak further (Fig. 5). At the same time, the emergence of a stronger SnS_2 (100) peak and a clearly distinguishable SnO_2 (211) peak at $2\theta = 52°$ indicates the formation of significant additional SnS_2 and SnO_2.

Since past work [53] shows that the XRD peaks of ZnS are almost the same as that of kesterite phase CZTS, Raman spectroscopy was used to confirm the formation of the kesterite CZTS. At 10 J/cm^2 (Fig. 6a) the major Raman peaks are SnS (220 cm^{-1}) [54] and SnS_2 (315 cm^{-1}) [54] and a minor CZTS peak at 288 cm^{-1} [55]. Increasing the fluence to 16 J/cm^2 (Fig. 6b) yields very significant characteristic peaks of kesterite CZTS at 288 and 328 cm^{-1} [55], and the disappearance of the SnS (220 cm^{-1}) peak. At 20 J/cm^2 (Fig. 6c) the CZTS A_1 mode peak considerably reduces. Further, significant SnS_2 peaks appear at 208 cm^{-1} and 315 cm^{-1} corresponding to the E_g mode and A_{1g} mode

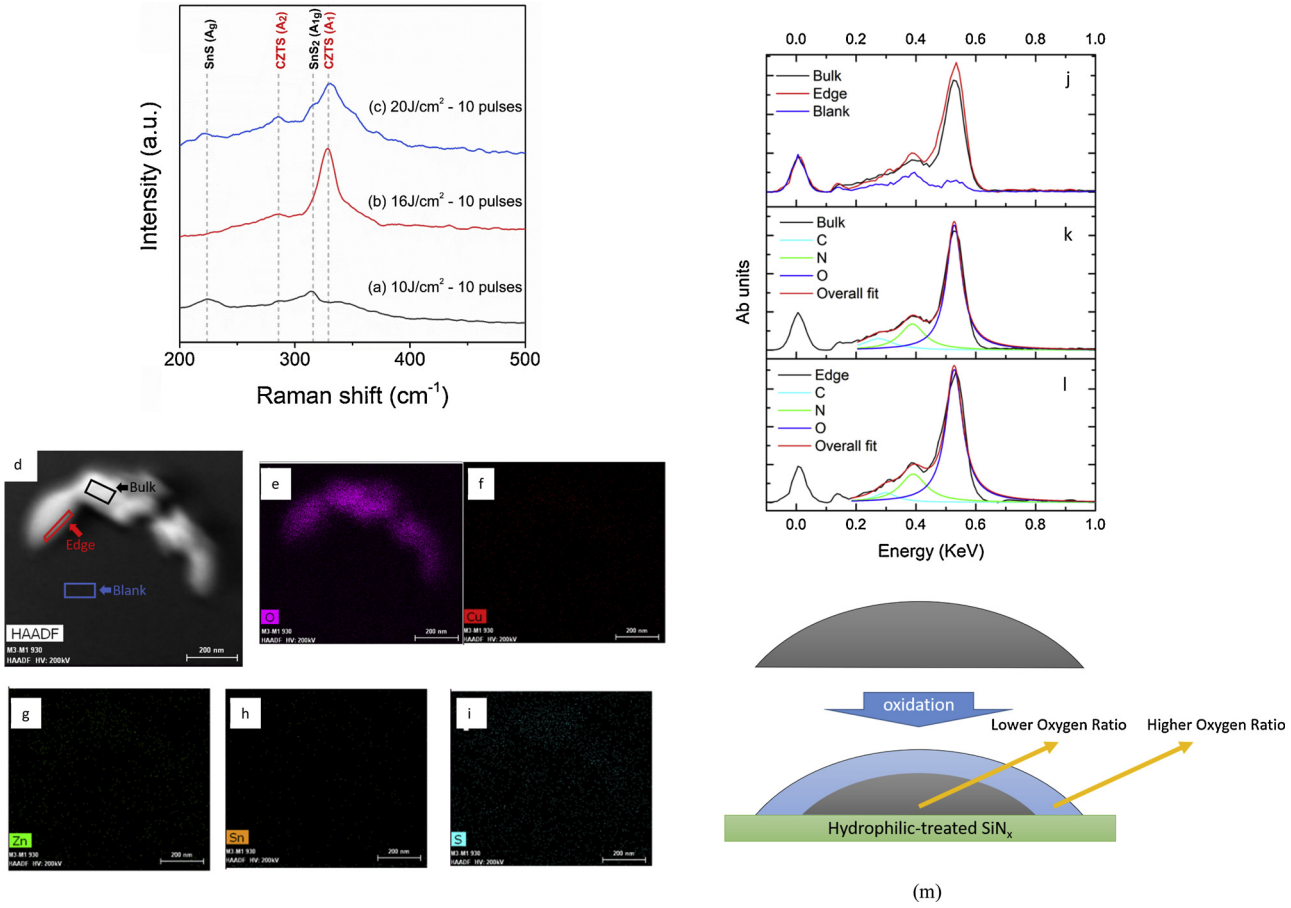

Fig. 6. Raman spectra of the IPL-sintered CZTS for fluence (a) 10 J/cm^2 (b) 16 J/cm^2 (c) 20 J/cm^2. (d) STEM image of the 20 J/cm2 IPL-sintered CZTS sample; (e–i) element-specific EDS mapping of O, Cu, Zn, Sn, and S; (*j*) EDS spectra from three different areas marked in (a); (k) deconvoluted EDS spectrum in bulk area with Lorentzian peak fitting; (l) deconvoluted EDS spectrum in edge area with Lorentzian peak fitting. (m) Schematic of core-shell structure of the CZTS film.

respectively. We note that ZnS peaks (352 cm^{-1} for TO mode and 271 cm^{-1} for LO mode) are not visible at any of these fluences, thus confirming the identification of CZTS (112) peaks seen in the XRD spectra. The absence of significant Cu_2SnS_3, Cu_7S_4, $Cu_{2-x}O$ or ZnO peaks in both the Raman spectra and XRD patterns show that these deleterious phases are not being formed in significant quantity.

One possible reaction pathway for the formation of CZTS from CuS, SnS and ZnS binary phases starts from the reaction of CuS phase with SnS to form Cu_2SnS_3 (reaction 1) [27], which reacts with ZnS to finally form CZTS (reaction 2) [56,57]. Further, the SnS can oxidize to create SnS_2 and SnO_2 (reaction 3) [58]. Combining the XRD and Raman spectra observations with these reaction pathways yields the following insights into how IPL fluence affects the formation of CZTS.

$$2CuS + SnS \rightarrow Cu_2SnS_3 \quad (1)$$

$$Cu_2SnS_3 + ZnS \rightarrow Cu_2ZnSnS_4 \quad (2)$$

$$2SnS + O_2 \rightarrow SnS_2 + SnO_2 \quad (3)$$

At 10 J/cm^2 some CZTS is formed via reactions (1) and (2) as indicated by the A_2 Raman peak, but its crystallinity is relatively low as shown in the XRD patterns, primarily due to the lower temperatures during IPL synthesis. This is supported by the relatively lesser grain growth compared to the as-deposited state, as seen in Fig. 7b–c where the inter-NP boundaries are still visible. Concurrently, the oxidation of some of the SnS to SnS_2 and SnO_2 occurs via reaction (3), as indicated by the A_{1g} Raman peak for SnS_2. However, the relative lack of significant crystalline XRD peaks of these by-products indicates their primarily amorphous nature.

As the film temperature increases for 16 J/cm^2 an even greater amount of SnS reacts (seen by disappearance of SnS Raman peaks) to form more crystalline CZTS via reactions (1–2) and relatively more amorphous SnS_2 via reaction (3) (shown by small XRD peaks). The observation of much sharper kesterite CZTS peaks in both the XRD and Raman spectra suggests that the SnS is preferentially contributing to the formation of CZTS rather than the formation of SnS_2. The lower FWHM of the primary CZTS XRD peak also agrees with the Raman spectra observation of greater crystalline CZTS formation. The greater increase in NP fusion and in grain size is confirmed by a simple visual observation of SEM images (e.g., Fig. 7b–e) which shows the disappearance of individual NP boundaries as compared to the lower fluence case. The TEM image in Fig. 7a confirms the formation of a nanocrystal structure with interplanar spacing of 0.32 nm that matches the CZTS (112) plane observed in the XRD spectra. Larger scale TEM images imaging (Fig. 7f) shows the absence of mesoscale porosity in the film. Further, both cross sectional SEM and AFM imaging show dense and continuous films with some small cracks, with a film thickness of ≈ 1 μm and surface roughness of 2.43 nm over a 10 μm × 10 μm scan area (Fig. 7g–h).

Increasing the fluence to 20 J/cm^2 increases the temperature even more and provides greater opportunity for conversion of SnS to SnS_2 via reaction (3), which results in SnS contributing lesser to CZTS formation by reactions (1–2). This is evidenced by the XRD spectra which shows increasingly crystalline SnS_2 and SnO_2 content relative to CZTS, and Raman peaks which show reduced CZTS A_1 mode peaks and appearance of more significant SnS_2 E_g and A_{1g} modes. STEM EDS mapping provides a more detailed identification of the phase composition for this fluence. The O:N ratios in bulk and edge regions are 2.966 and 3.256

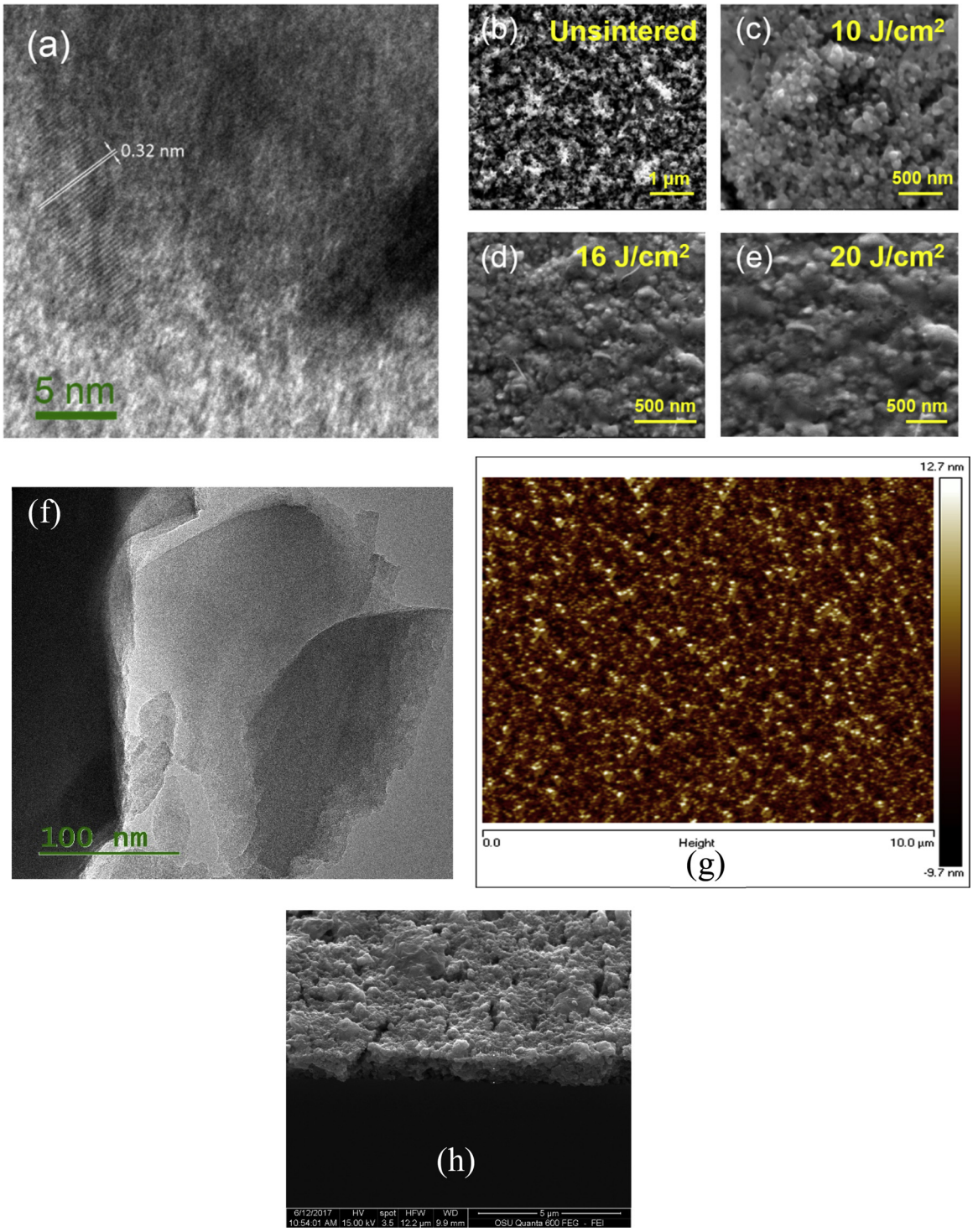

Fig. 7. (a) High resolution TEM image. SEM images of the films. (b) As deposited. (c) 10 J/cm^2 (d) 16 J/cm^2 (e) 20 J/cm^2. (f) Larger scale TEM image (g) AFM scan of film surface (h) cross-section of film. All shown for CZTS sample for IPL fluence 16 J/cm^2.

respectively, showing a roughly 10% increase in oxygen content at the edge regions. This indicates that the CZTS film has a core-shell structure with the oxide shell contribute more oxygen counts at the edge area of the composite sample (Fig. 6m). This implies that the region of the CZTS film near the glass substrate will have lesser oxygen content as compared to the top part of the CZTS film.

Based on these observations 16 J/cm^2 is identified as the optimal fluence for obtaining pure-phase kesterite CZTS films with high crystallinity, and supra-optimal fluence leads to the formation of a composite film with relatively greater SnO_2 and SnS_2 phases in addition to CZTS. The increase in SnO_2 and SnS_2 content with increasing fluence is due to increasing film temperature and greater thermodynamic favorability for oxidation of SnS, as observed in air sintering of CuS-ZnS-SnS mixtures [23]. This past work has also shown the formation of $Cu_{2-x}O$ and SnO_2 at oven annealing temperatures below 400°C. Our IPL results do not show any copper oxide formation, and yield significant formation of SnO_2 only when temperatures are well above 400°C. This is because the milliseconds scale pulse duration and shorter total

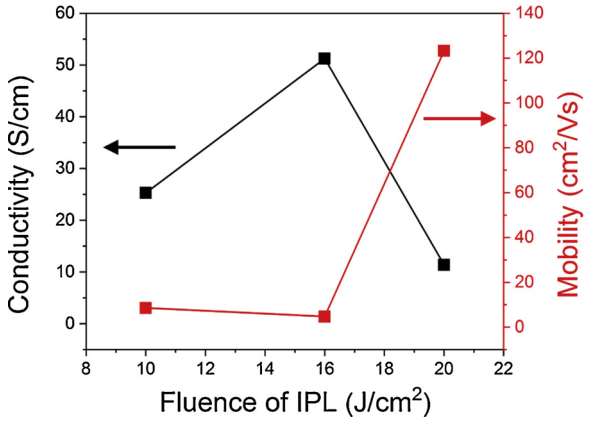

Fig. 8. Electrical conductivity and carrier mobility of CZTS films after IPL synthesis.

synthesis time does not allow enough time for significant oxidation of the CuS phase in the film, as supported by observations in IPL of CuS-only NP films [27]. Further, the formation of kesterite rather than wurtzite CZTS is also due to the high speed of the reaction and the resulting lack of formation of copper sulfide intermediaries, which retards the formation of the wurtzite phase [59].

3.2. Electrical, optical and photocatalytic properties

The average Hall coefficients of the films were 0.34, 0.1 and 10.8 corresponding to increasing IPL fluence, showing that effectively p-type films are formed. Conductivity σ in a p-type material is given $\sigma = p \cdot e \cdot \mu_h$ where p is the hole concentration, e is the elementary charge, and μ_h is the hole mobility.

The increase in pulse fluence from 10 to 16 J/cm^2 increases conductivity by nearly twice (Fig. 8) but with a relatively smaller change in mobility. This suggests a significant increase in hole concentration with greater IPL induced formation and crystallization of CZTS. At the supra-optimal fluence of 20 J/cm^2 the conductivity decreases drastically but the mobility increases equally remarkably (about 26 times, Fig. 8), indicating significant reduction in hole concentration. This is contrast to conventional air sintering of CZTS films below 500°C which shows increasing conductivity with greater sintering temperature, often due to formation of copper rich sulfides [25].

No such copper rich sulfides are observed in our experiments. We further note that the conductivity achieved after IPL synthesis is comparable or greater than that from conventional sintering performed on the time scale of hours, often inside a controlled atmosphere (e.g., 1.72 S/cm by oven annealing of pre-synthesized CZTS nanoparticles [60] and 10 S/cm by RF sputtering [15]). Further, the carrier mobility in the case of the supra-optimal fluence is also several orders of magnitude greater than that from such annealing approaches (e.g., 2.56 cm^2/Vs from oven annealing of pre-synthesized CZTS nanoparticles [60] and 1.419 cm^2/Vs from RF sputtering [15]). This can be attributed to the formation of greater SnO_2 and SnS_2 (which are intrinsically n-type) at the expense of intrinsically p-type kesterite CZTS at the supra-optimal fluence. This formation of internal p-n junctions in the film reduces the hole concentration and creates internal electric fields which reduce carrier recombination, thus increasing the carrier mobility [61].

The measured UV–vis absorbance spectrum of the films (Fig. 9a) and the IPL power spectrum (Fig. S1a, Supplementary Information) show that the as-deposited films absorb nearly 80% of the xenon lamp power. Interestingly, the film at a low fluence of 10 J/cm^2 consisting of relatively amorphous CZTS and SnS_2-SnO_2 by-products exhibits significantly lower IPL absorption as compared to the as-deposited film. When enough energy is supplied (i.e., 16 J/cm^2) the IPL absorption increases due to crystallization of CZTS but does not change very significantly with even greater fluence (20 J/cm^2). This indicates that at a given fluence the absorption of IPL, which is responsible for the temperature rise and formation of CZTS, initially reduces as the film goes through the lower temperature portion of the pulse and then increases and levels off as the temperature increases enough to crystallize CZTS. This dynamic evolution of IPL absorption contrasts with that seen in IPL sintering of metallic NPs, where the IPL absorption monotonically reduces with the evolution of NP fusion.

The direct band gap energy of the as-deposited and sintered CZTS thin films is shown in Fig. 9c, as calculated using Tauc's plots (Fig. 9b). At 10 J/cm^2 fluence, the band gap reduces to 1.17 eV due to the low crystallinity of the CZTS and the quantum confinement effect [62]. At 16 J/cm^2 fluence the band gap increases to 1.42 eV and then decreases slightly to 1.33 eV at 20 J/cm^2 fluence. Besides the quantum confinement effect, the optical band gap is also affected by the charge carrier concentration, as per the Burstein-Moss effect [63]. This phenomenon dictates that the optical band gap of a semiconductor increases with greater carrier concentration because the absorption edge is pushed to higher energies. In our experiments the IPL fluence affects the band gap with the same qualitative trend as it affects the carrier concentration (Fig. 8), suggesting that the Burstein-Moss effect can explain the observed dependence of band gap on IPL fluence. The band gap energy of the CZTS film synthesized at 16 J/cm^2 corresponds well to that for bulk kesterite CZTS in literature [64] and is close to that obtained from recent works on Pulsed Laser Deposition (1.47 eV [14]) and conventional annealing of pre-synthesized CZTS nanoparticles [29].

Fig. 10a–c shows the UV–vis absorption spectra of MB at varying sampling times during the photocatalysis tests. As a model organic pollutant, MB is stable under visible light irradiation if no photocatalysts are involved. The temporal reduction in the characteristic MB absorption peak at 664 nm in Fig. 10 shows the photocatalytic degradation of MB molecules by the CZTS film. It was not possible to measure photocatalysis for the as-deposited case since the films detached from the substrate upon immersion into the MB solution. Most literature on CZTS photocatalytic research is focused on the nano- or micro- particles dispersed in liquid, whereas our use of solid films is more advantageous from an application point of view. Further the efficiency measurement is typically done for a wide ranges of incident light during MB degradation. This makes it infeasible to directly compare our work to literature. At the same time, our sample uses about 1.8 mg of precursor binary NPs as compared to the typical use of 10˜50 mg weight of NPs in literature. The mechanism for the photocatalytic degradation is described by Eqs. (4–10) and is illustrated in Fig. 10e [66]. Eqs. (4–10) illustrate the mechanisms involved in the MB degradation. The MB degradation reaction mainly relies on the hydroperoxyl and hydroxyl radicals (Equation 9 & 10), with possible direct oxidation by photogenerated hole (Eq. 5). For cationic dye as MB, the chance of MB cations directly attaching to the positive charged CZTS surface is relatively low, and most MB cations will prefer negative charged SnO_2 (or SnS_2) surface.

Fig. 10d shows the temporal evolution of normalized MB concentration, i.e., C/C_0, as derived from the absorption curves in Fig. 10a–c. The standard deviation shown corresponds to the error between measurement after synthesis as compared to one year after synthesis. Over the 4 h of testing the films synthesized at 16 J/cm^2 fluence show an additional 15% reduction in C/C_0 (or increase in photocatalysis) as compared to the 10 J/cm^2 fluence films. This is due to increased carrier concentration (Fig. 8) and greater crystallization and NP fusion (Figs. 5 and 7) which prevent carrier recombination. Interestingly, the films synthesized at 20 J/cm^2 yield an additional 20% drop in C/C_0 even compared to the 16 J/cm^2 fluence films. This increased catalytic efficiency is despite the relative increase in SnO_2/SnS_2 at the expense of the CZTS content in the film. The k_{app} for fluence 10, 16 J/cm^2, and 20 J/cm^2 was 0.0011, 0.0023, and 0.0046 min^{-1} respectively with very little change in photocatalytic behavior over the timespan of one year.

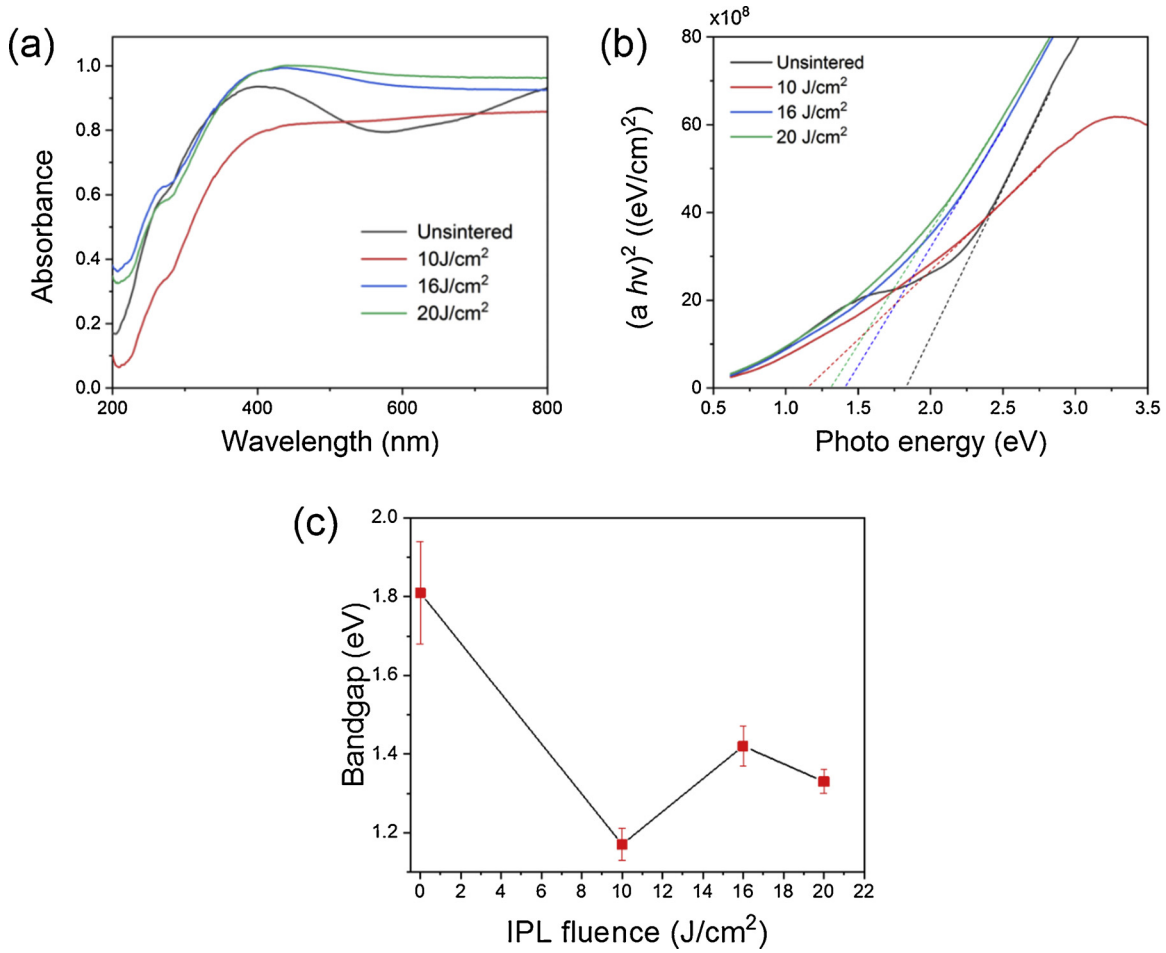

Fig. 9. (a) UV–vis absorption spectra and (b) Tauc's plots for IPL synthesized CZTS films. Here, $(ah\nu)^2 = A\,(E_g - h\nu)$, where α is the absorption coefficient (in cm^{-1}), $h\nu$ is the photon energy (unit in eV), A is a constant, and E_g is the direct optical band gap (unit in eV) [25,65]. (c) Optical band gap for IPL synthesized and as-deposited CZTS films.

$$Cu_2ZnSnS_4 \xrightarrow{visible\ light} Cu_2ZnSnS_4\,(e_{cb}^- + h_{vb}^+) \quad (4)$$

$$h_{vb}^+ + \text{MB} \rightarrow \text{degraded products} \quad (5)$$

$$h_{vb}^+ + H_2O \rightarrow \bullet OH + H^+ \quad (6)$$

$$e_{cb}^- + O_2 \rightarrow \bullet OO^- \quad (7)$$

$$\bullet OO^- + H^+ \rightarrow \bullet OOH \quad (8)$$

$$\bullet OH + \text{MB} \rightarrow \text{degraded products} \quad (9)$$

$$\bullet OOH + \text{MB} \rightarrow \text{degraded products} \quad (10)$$

Fig. 11 suggests the mechanism of radical generation based on the band structure of CZTS/SnO_2 and SnS_2 [67,68]: on n-type side (SnO_2 or SnS_2), dissolved O_2 is converted to hydroperoxyl radical (Eqs. 7 & 8); while on p-type side (CZTS), hydroxyl ion is converted to hydroxyl radical (Eq. 6). So, the reaction does need water as a source for the photogenerated radicals, and the MB degradation is not directly occurring by the electron-hole pair although the electron-hole generation plays a key role. On the other hand, the radicals are highly reactivity, transient, and short mean free path. The negative charged n-type SnO_2 (or SnS_2) can help attracting MB to the radical concentrated surface, and promote the degradation. The major limitations to photocatalytic activity are recombination of optically induced electron-hole pairs and the back-reaction of intermediate species. As discussed earlier, the 20 J/cm^2 fluence films contain greater crystalline SnO_2 and SnS_2 relative to crystalline CZTS than the films synthesized with lower fluence. We propose that in these 20 J/cm^2 films the intrinsically n-type SnS_2 and SnO_2 form internal p-n junctions with the intrinsically p-type CZTS. The resultant creation of an internal electric field effectively mitigates electron-hole recombination [61]. As illustrated in Fig. 11, the photogenerated electron-hole pairs are quickly separated by the space charge region electric field, and the electrons generated in CZTS are rapidly transferred to the SnO_2/SnS_2 side, creating reduction sites for photocatalysis and leaving holes and oxidation sites on the CZTS side. With lesser carrier recombination occurring a greater fraction of the incident optical energy is used in photocatalysis, thus increasing the photocatalytic efficiency. We note that the higher charge carrier mobility observed at this fluence (Fig. 8) can also be explained by the formation of such internal p-n junctions, as discussed earlier, which further supports our hypothesis.

4. Conclusion

This work successfully demonstrates rapid and ambient-condition IPL induced photochemical synthesis of quaternary CZTS films from binary CuS, ZnS, SnS NP mixtures. The effect of IPL on the photocatalytic activity of the films is characterized and explained in terms of the underlying reaction pathways governing the film composition and the photocatalytic degradation. The key advances made are as follows.

Tuning the IPL fluence produces films with variable compositions, yielding crystalline kesterite CZTS films or composite films with relatively greater amount of SnO_2 and SnS_2 at the expense of CZTS. In all the cases the formation of undesirable secondary phases such as Cu_2SnS_3 and Cu_7S_4 is avoided. This is due to the high-energy and pulsed

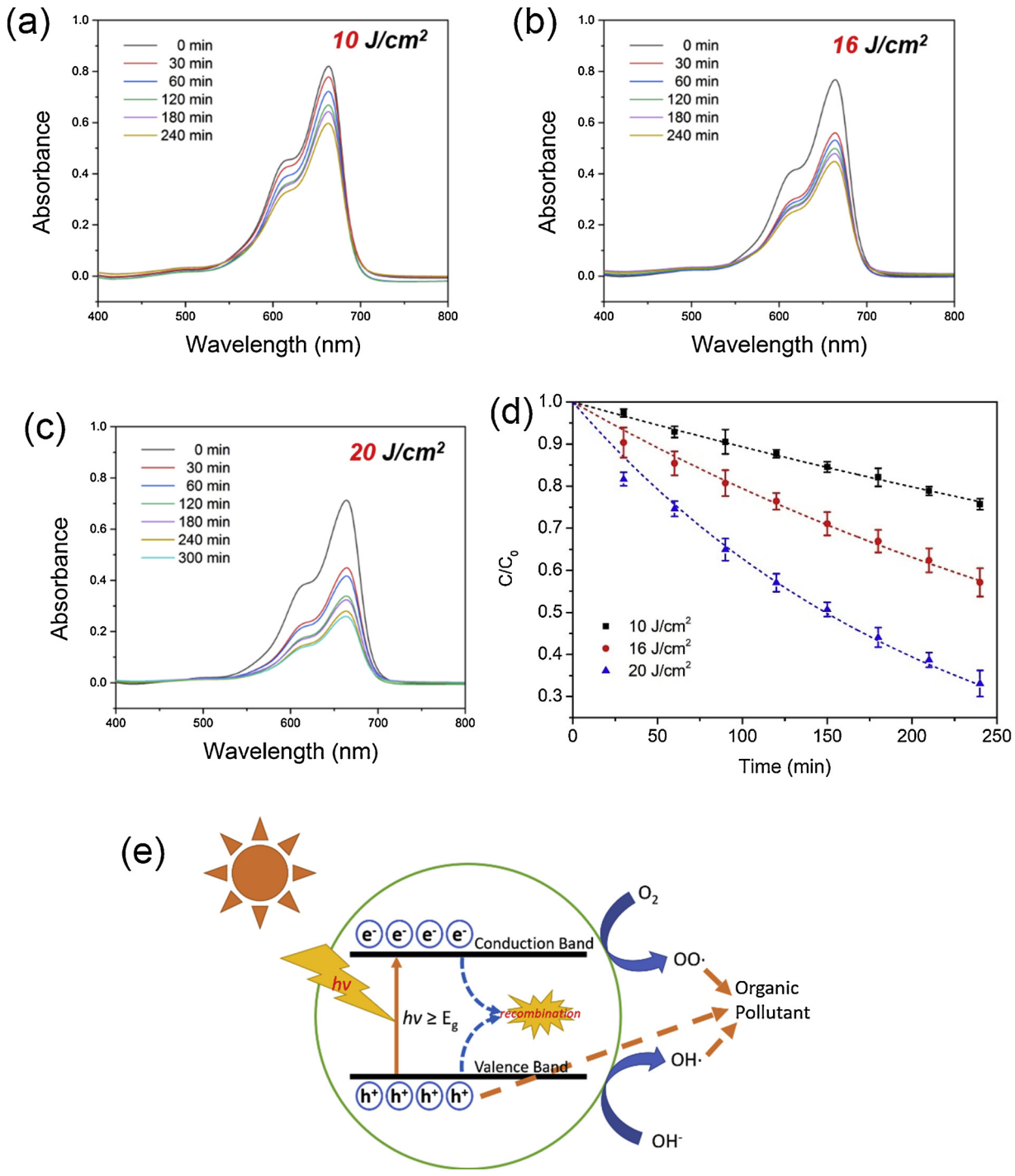

Fig. 10. Photocatalytic breakdown of methylene blue by CZTS films. UV–vis absorbance spectra of the MB solution at different sampling times using the prepared CZTS films as a photocatalyst; IPL fluence of (a) 10 J/cm^2 (b) 16 J/cm^2 (c) 20 J/cm^2. (d) Degradation curves for MB with IPL synthesized CZTS films (C_0 is the initial concentration of MB; C is the concentration of MB at arbitrary time t during photocatalysis). Standard deviation is between measurements taken one year apart. (e) Schematic of charge carrier separation and photocatalytic contaminant decomposition by CZTS under visible light irradiation. (For interpretation of the references to colour in this figure legend, the reader is referred to the web version of this article).

nature of IPL which limits the formation of copper sulfide intermediaries, and is significant because such intermediaries are typically formed in conventional air annealing of pre-synthesized CZTS NP films.

The CZTS films produced at the optimal fluence (16 J/cm^2) have electrical conductivity similar to or greater than less scalable and more cumbersome approaches like Pulsed Laser Deposition, RF sputtering and conventional annealing. The optical band gap is also comparable to these synthesis methods. The films produced at supra-optimal fluence show several orders of magnitude greater carrier mobility than oven annealing and RF sputtering. Further, the photocatalytic efficiency increases even though the SnO_2/SnS_2 content is increasing at the expense of the CZTS content. This is due to the formation of internal p-n junctions in the film that restrict carrier recombination.

The total IPL synthesis time does not exceed 19 s (Table 1), while the corresponding peak temperatures are 350°C and 430°C for the optimal and supra-optimal fluences. In comparison, the typical sintering conditions reported for fabrication of kesterite CZTS films involves similar or slightly greater temperatures but orders of magnitude greater

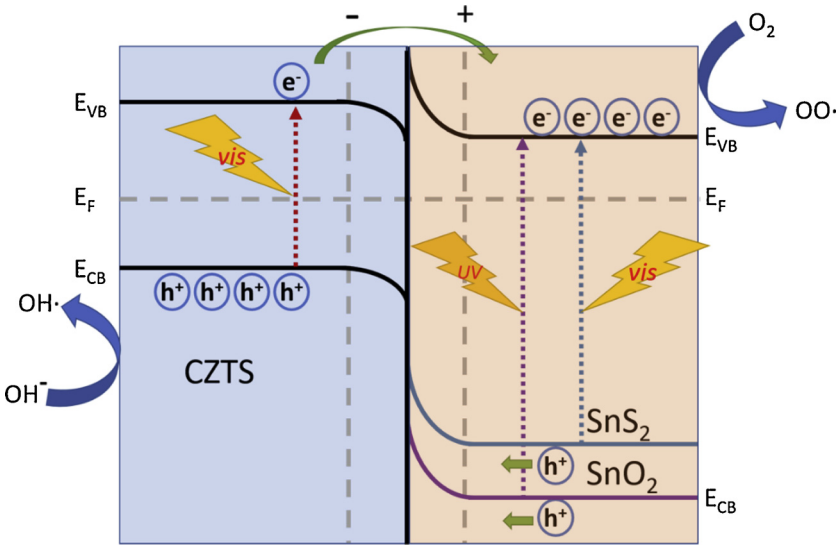

Fig. 11. Schematic of p-n junction band structure and electron-hole pairs separation in CZTS-SnO_2/SnS_2 p-n junction photocatalyst. By coupling *p*-type CZTS (E_g = 1.4 eV) with *n*-type SnO_2 ($E_g \approx$ 3.6 eV) and SnS_2 ($E_g \approx$ 2.1 eV) the separated charges will be rapidly transferred across the interface to reduce carrier recombination and increase photocatalytic efficiency.

time (e.g., 400–500℃ for 30 min to 1 h [25,69] or 200℃ for 4 h [70]). The synthesis time in IPL is even shorter than in the high temperature Rapid Thermal Processing method, which still takes about 5–10 minutes [26]. This enables IPL to have a significantly lower energy budget during fabrication. Since the large optical footprint of IPL can be used without influencing the temperature rise, IPL synthesis is also highly scalable.

This advance presents an attractive strategy for scalable fabrication of CZTS films for photocatalysis. We note that using this process for fabrication of solar cells, while potentially advantageous, will require it to extended to obtain films with desired thickness and more tightly controlled phase and microstructure. The demonstrated approach also envisages new opportunities for scalable and in-situ bottom-up fabrication of additional multinary chalcogenide films (e.g., $CuInS_2$, $CuInSe_2$, $AgInSe_2$ and CIGSe). When combined with the existing capabilities of inkjet printing to spatially arrange NPs of different materials by design, this approach may also enable discovery of new chalcogenide-composite materials for various applications.

Declaration of Competing Interest

The authors declare that they have no known competing financial interests or personal relationships that could have appeared to influence the work reported in this paper.

Acknowledgement

This work was supported by the National Science Foundation, USA, grant CMMI #1809289.

Appendix A. Supplementary data

Supplementary material related to this article can be found, in the online version, at doi:https://doi.org/10.1016/j.materresbull.2019.110645.

References

[1] D.B. Mitzi, O. Gunawan, T.K. Todorov, K. Wang, S. Guha, Sol. Energy Mater. Sol. Cells 95 (2011) 1421–1436.
[2] H. Katagiri, K. Jimbo, W.S. Maw, K. Oishi, M. Yamazaki, H. Araki, A. Takeuchi, Thin Solid Films 517 (2009) 2455–2460.
[3] C. Ros, T. Andreu, S. Giraldo, V. Izquierdo-Roca, E. Saucedo, J.R. Morante, ACS Appl. Mater. Interfaces 10 (2018) 13425–13433.
[4] Z. Wang, G.P. Demopoulos, ACS Appl. Mater. Interfaces 7 (2015) 22888–22897.
[5] R. Aruna-Devi, M. Latha, S. Velumani, J. Santoyo-Salazar, J. Santos-Cruz, Mater. Res. Bull. 111 (2019) 342–349.
[6] L. Kang, Z. Zhang, J. Shi, R. Yan, J. Zhang, Mater. Res. Bull. 113 (2019) 31–37.
[7] B. Long, S. Cheng, D. Ye, C. Yue, J. Liao, Mater. Res. Bull. 115 (2019) 182–190.
[8] A. Tumbul, A. Göktaş, M.Z. Zarbali, F. Aslan, Mater. Res. Express 5 (2018) 066408.
[9] L. Rovelli, S.D. Tilley, K. Sivula, ACS Appl. Mater. Interfaces 5 (2013) 8018–8024.
[10] T. Yoshida, A. Yamaguchi, N. Umezawa, M. Miyauchi, J. Phys. Chem. C 122 (2018) 21695–21702.
[11] S.A. Phaltane, S.A. Vanalakar, T.S. Bhat, P.S. Patil, S.D. Sartale, L.D. Kadam, J. Mater. Sci. Mater. Electron. 28 (2017) 8186–8191.
[12] X. Yu, A. Shavel, X. An, Z. Luo, M. Ibáñez, A. Cabot, J. Am. Chem. Soc. 136 (2014) 9236–9239.
[13] N. Nakayama, K. Ito, Appl. Surf. Sci. 92 (1996) 171–175.
[14] J. Hu, H. Xiao, G. Liang, Z. Su, P. Fan, X. Lin, J. Alloys Compd. 765 (2018) 888–893.
[15] N. Akcay, E.P. Zaretskaya, S. Ozcelik, J. Alloys Compd. 772 (2019) 782–792.
[16] Y.-P. Lin, Y.-F. Chi, T.-E. Hsieh, Y.-C. Chen, K.-P. Huang, J. Alloys Compd. 654 (2016) 498–508.
[17] K. Ito, T. Nakazawa, J. Appl. Phys. 27 (1988) 2094.
[18] B.A. Williams, N.D. Trejo, A. Wu, C.S. Holgate, L.F. Francis, E.S. Aydil, ACS Appl. Mater. Interfaces 9 (2017) 18865–18871.
[19] B.A. Williams, A. Mahajan, M.A. Smeaton, C.S. Holgate, E.S. Aydil, L.F. Francis, ACS Appl. Mater. Interfaces 7 (2015) 11526–11535.
[20] J.W. Cho, A. Ismail, S.J. Park, W. Kim, S. Yoon, B.K. Min, ACS Appl. Mater. Interfaces 5 (2013) 4162–4165.
[21] G. Wang, W. Zhao, Y. Cui, Q. Tian, S. Gao, L. Huang, D. Pan, ACS Appl. Mater. Interfaces 5 (2013) 10042–10047.
[22] W. Zhao, F. Yu, S.F. Liu, ACS Appl. Mater. Interfaces 11 (2019) 634–639.
[23] K.J. Kim, C.Q. Pan, S. Bansal, R. Malhotra, D.H. Kim, C.H. Chang, Sustain. Energy Fuels 1 (2017) 267–274.
[24] J. Zhang, Y. Yang, J. Zhao, Z. Dai, W. Liu, C. Chen, S. Gao, D. Golosov, S. Zavadski, S. Melnikov, Mater. Res. Bull. (2019) 110529.
[25] Y. Wang, Y. Huang, A.Y. Lee, C.F. Wang, H. Gong, J. Alloys Compd. 539 (2012) 237–241.
[26] S.M. Pawar, A.I. Inamdar, B.S. Pawar, K.V. Gurav, S.W. Shin, X. Yanjun, S.S. Kolekar, J.-H. Lee, J.H. Kim, H. Im, Mater. Lett. 118 (2014) 76–79.
[27] M. Dexter, Z. Gao, S. Bansal, C.-H. Chang, R. Malhotra, Sci. Rep. 8 (2018) 2201.
[28] H.R. Jung, S.W. Shin, K.V. Gurav, M.P. Suryawanshi, C.W. Hong, H.S. Yang, J.Y. Lee, J.H. Moon, J.H. Kim, Ceram. Int. 41 (2015) 13006–13011.
[29] E. Indubala, S. Sarveshvaran, V. Sudha, A.Y. Mamajiwala, S. Harinipriya, Sol. Energy 173 (2018) 215–224.
[30] K. Yu, E.A. Carter, Chem. Mater. 27 (2015) 2920–2927.
[31] C.-h. Chang, B. Stanbery, A. Morrone, A. Davydov, T. Anderson, Mrs Proc. 485 (1997) 163.
[32] S. Wünscher, R. Abbel, J. Perelaer, U.S. Schubert, J. Mater. Chem. C 2 (2014) 10232–10261.
[33] M. Sygletou, C. Petridis, E. Kymakis, E. Stratakis, Adv. Mater. 29 (2017) 1700335.
[34] S. Bansal, R. Malhotra, Nanotechnology 27 (2016) 495602.
[35] H.-J. Hwang, R. Malhotra, ACS Appl. Mater. Interfaces 11 (2019) 3536–3546.
[36] S.-H. Park, H.-S. Kim, Thin Solid Films 550 (2014) 575–581.
[37] H.-J. Hwang, K.-H. Oh, H.-S. Kim, Sci. Rep. 6 (2016) 19696.
[38] R. Dharmadasa, I. Dharmadasa, T. Druffel, Adv. Eng. Mater. 16 (2014) 1351–1361.
[39] R. Dharmadasa, B. Lavery, I. Dharmadasa, T. Druffel, ACS Appl. Mater. Interfaces 6 (2014) 5034–5040.
[40] H.-J. Hwang, H.-S. Kim, J. Nanosci. Nanotechnol. 15 (2015) 5028–5034.
[41] S.R. Dhage, H.T. Hahn, J. Phys. Chem. Solids 71 (2010) 1480–1483.
[42] B.W. Lavery, S. Kumari, H. Konermann, G.L. Draper, J. Spurgeon, T. Druffel, ACS Appl. Mater. Interfaces 8 (2016) 8419–8426.
[43] S.R. Dhage, H.-S. Kim, H.T.J.J.o.E.M. Hahn, 40 (2011) 122-126.
[44] B.-Y. Wang, T.-H. Yoo, Y.-W. Song, D.-S. Lim, Y.-J. Oh, ACS Appl. Mater. Interfaces

5 (2013) 4113–4119.
[45] T.-H. Yoo, S.-J. Kwon, H.-S. Kim, J.-M. Hong, J.A. Lim, Y.-W. Song, RSC Adv. 4 (2014) 19375–19379.
[46] K. Tetzner, Y.-H. Lin, A. Regoutz, A. Seitkhan, D.J. Payne, T.D. Anthopoulos, J. Mater. Chem. C 5 (2017) 11724–11732.
[47] Q. Guo, G.M. Ford, W.-C. Yang, B.C. Walker, E.A. Stach, H.W. Hillhouse, R. Agrawal, J. Am. Chem. Soc. 132 (2010) 17384–17386.
[48] Q. Guo, H.W. Hillhouse, R. Agrawal, J. Am. Chem. Soc. 131 (2009) 11672–11673.
[49] M. Dexter, A. Pfau, Z. Gao, G.S. Herman, C.-h. Chang, R. Malhotra, Nanotechnology 29 (2018) 505205.
[50] T. Hurma, S. Kose, Optik 127 (2016) 6000–6006.
[51] W.G. Nilsen, Phys. Rev. 182 (1969) 838–850.
[52] M. Gurubhaskar, N. Thota, M. Raghavender, Y.P. Venkata Subbaiah, G. Hema Chandra, K.T. Ramakrishna Reddy, Nano 12 (2017) 1750120.
[53] S.W. Shin, S.M. Pawar, C.Y. Park, J.H. Yun, J.-H. Moon, J.H. Kim, J.Y. Lee, Sol. Energy Mater. Sol. Cells 95 (2011) 3202–3206.
[54] Y. Jayasree, U. Chalapathi, V.S. Raja, Thin Solid Films 537 (2013) 149–155.
[55] P.A. Fernandes, P.M.P. Salome, A.F. da Cunha, J. Alloys Compd. 509 (2011) 7600–7606.
[56] E. Lund, H. Du, W. Hlaing Oo, G. Teeter, M.A. Scarpulla, J. Appl. Phys. 115 (2014) 173503.
[57] A. Fairbrother, X. Fontané, V. Izquierdo-Roca, M. Espíndola-Rodríguez, S. López-Marino, M. Placidi, L. Calvo-Barrio, A. Pérez-Rodríguez, E. Saucedo, Sol. Energy Mater. Sol. Cells 112 (2013) 97–105.
[58] H. Du, F. Yan, M. Young, B. To, C.-S. Jiang, P. Dippo, D. Kuciauskas, Z. Chi, E.A. Lund, C. Hancock, J. Appl. Phys. 115 (2014) 173502.
[59] Z. Li, A.L.K. Lui, K.H. Lam, L. Xi, Y.M. Lam, Inorg. Chem. 53 (2014) 10874–10880.
[60] F. Yang, R. Ma, W. Zhao, X. Zhang, X. Li, J. Alloys Compd. 689 (2016) 849–856.
[61] L. Li, P.A. Salvador, G.S. Rohrer, Nanoscale 6 (2014) 24–42.
[62] K. Moriya, J. Watabe, K. Tanaka, H. Uchiki, Physica Status Solidi C 3 (2006) 2848–2852.
[63] Y. Peter, M. Cardona, Fundamentals of Semiconductors: Physics and Materials Properties, Springer Science & Business Media, 2010.
[64] S. Ahn, S. Jung, J. Gwak, A. Cho, K. Shin, K. Yoon, D. Park, H. Cheong, J.H. Yun, Appl. Phys. Lett. 97 (2010) 021905.
[65] J. Tauc, Mater. Res. Bull. 3 (1968) 37–46.
[66] P. Vas-Umnuay, K.-J. Kim, D.-H. Kim, C.-H. Chang, CrystEngComm 17 (2015) 2827–2836.
[67] S. Huang, W. Luo, Z. Zou, J. Phys. D Appl. Phys. 46 (2013) 235108.
[68] A. Duta, L. Andronic, A. Enesca, Catal. Today 300 (2018) 18–27.
[69] M. Dhanasekar, S.V. Bhat, Appl. Surf. Sci. 418 (2017) 194–198.
[70] T.K. Chaudhuri, D. Tiwari, Sol. Energy Mater. Sol. Cells 101 (2012) 46–50.